A IONAL APP OXIMA ION FO OMOG APHIC ECON C ION

AT HE EY D G EG Y BEY I A D CA Z

Abstract. us opt a at on appro at ons o pro ct on ata co ct n X a to og ap to prov a g r so ut on n r t assu p t on t at t o ct o nt r st s scr unct ons t u p scont nu t s or ac pro ct on construct ts at on appro at on t a s a n ar opt a nu r o t r s ora g v n accura c t r s o sa o s us to aug nt t asur ata ou t nu r o a a a sa p s n ac pro ct on or qu a nt t n ou t a n o t r Four r trans or a so v op a n ast poa r coor nat Four r a n a go r t us s our non n ar appro at on o pro ct on ata n a atura a

s ng aug nt pro ct ons o t pp og a n p anto prov a co par son t n t n a gor t an t stan r F t r Ba c ro ct on FB a gor t onstrat t a t t r construct a g a s prov r so ut on t out a t on a art a cts n a r s a rp trans t ons n t a g

1. Introduction

As perceptively noted in [29], despite the development of many new algorithms for the inversion of the Radon transform, the quality of image reconstruction (in e.g., X-ray tomography) has not improved noticeably when compared with the output of the traditional Filtered Back-Projection (FBP) algorithm (see, for example [28]). This lack of improvement in image quality may be traced to the fact that the signal model for collected data is subject to the Nyquist sampling criterion. Since we are typically interested in reconstructing piece-wise continuous objects, the collected a (periodic) signal allows us, in principle, to recover its entire Fourier series from a small number of samples. In practice, even though the presence of noise limits such a recovery, a rational model still outperforms models based on the Nyquist sampling criterion. For objects with a limited number of isolated singularities, optimal rational approximations of projection data yield a significant improvement in resolution without introducing artifacts near singularities.

where $n = 0, \ldots, N-1$. Computing the DFT of $g\left(\frac{n}{N}\right)$, $n = 0, \ldots, N-1$,

$$\hat{g}_j = \frac{1}{N} \sum_{n=0}^{N-1} g\left(\frac{n}{N}\right) e^{-2\pi i n j/N}, \quad j = 0, \ldots, N-1,$$

we obtain

$$\hat{g}_j = \sum_{m=1}^{M} \frac{w_m}{1 - e^{-\eta_m N}} e^{-\eta_m j} + \sum_{m=1}^{M} \frac{\overline{w}_m}{1 - e^{-\overline{\eta}}} \tag{2.4}$$

and the operator K (applied to each projection separately)

$$(Kf)(s) = \frac{1}{2}\int_{\mathbb{R}} |\rho|\, \hat{f}(\rho)\, e^{2\pi i\rho s} d\rho.$$

Since multiplication by $|\rho|$ is an unbounded operator, in practice it is replaced by its band-limited approximation,

$$(Kf)(s) = \frac{1}{2}\int_{\mathbb{R}} |\rho|\, W(\rho)\, \hat{f}(\rho)\, e^{2\pi i\rho s} d\rho = \int_{\mathbb{R}} k(s-t) f(t) dt,$$

where

$$k(t) = \frac{1}{2}\int_{\mathbb{R}} |\rho|\, W(\rho)\, e^{-2\pi i\rho t} d\rho.$$

In FBP algorithms a typical choice for $|\rho|\, W(\rho)$ and, therefore $k(t)$, is the Shepp-Logan filter (see e.g., [28] for details). Since any filter modifies the measured data within its bandlimit, our goal is to first extend the bandlimit of the data so that when we apply the filter (see Algorithm 5.1), its impact on the measured data (within its original bandlimit) is reduced.

We also have from (3.1) the Fourier slice theorem,

$$\hat{u}(\rho\nu) = \int_{\mathbb{R}^2} u(\mathrm{x}) e^{-2\pi i\rho\nu\cdot\mathrm{x}} d\mathrm{x} = \int_{\mathbb{R}} (Ru)(s,\nu)\, e^{-2\pi i\rho s} ds,$$

which we use to build a fast and accurate Fourier domain reconstruction algorithm as an alternative to FBP. In this paper we only examine the so-called parallel beam tomography, i.e. the most simple geometry for the tomographic reconstruction problem. However, the methods used in this paper are applicable to other, more complex geometries, such as fan beam tomography.

3.2. uadratures for t e d s In order to have an accurate and fast reconstruction algorithm in the Fourier domain, we construct, for any user-specified accuracy $\epsilon > 0$, quadratures for integration (in polar coordinates) in the Fourier domain. Following [3, 4], we discretize integrals using quadratures for band-limited exponentials. In the radial variable these quadratures integrate exponentials against the weight $|\rho|$. In the angular variable we integrate using the trapezoidal rule.

Let us first examine the behavior of the Fourier transform of a real function supported within the box $B = [-1,1]\times[-1,1]$.

Propos t on Consider a real function f supported in B such that, in polar coordinates, $\hat{f}(c\rho,\theta)$, $\theta \in [0,2\pi]$, is negligible for $\rho > 1$, where $c > 0$ is the bandlimit. Extending the integration domain to a spatial disk of radius $\sqrt{2}$ containing B, we write

$$\hat{f}(c\rho,\theta) = \int^{2\pi}\int^{\sqrt{2}} f(r,\phi) e^{-icr\rho\cos\theta-\varphi}\, r\,dr\,d\phi = \sum_{l\in\mathbb{Z}} q_l(c\rho)\, e^{i\theta l},$$

where

$$q_l(c\rho) = \frac{1}{2\pi}\int^{2\pi} \hat{} \; {}_{2}$$

$$\left|\hat{f}(c\rho,\theta) - \sum_{l=-L}^{L} q_l(c\rho)\, e^{i\theta l}\right| \le \epsilon, \quad 0 \le \rho \le 1 \tag{3.2}$$

where

$$L \ge \max\left(7, e\sqrt{2}c, \log_2\left(2\|f\|_\infty \epsilon^{-1}\right)\right). \tag{3.3}$$

For the proof see Appendix 8. A similar observation was made in [27, 28] in the context of sampling for tomographic reconstruction algorithms.

Since the function f is real and $(\rho, \theta + \pi)$ and $(-\rho, \theta$

+

+

+

+

of the disk-to-disk mapping since, inter alia, for the square-to-disk case no ordinary differential equation is available to compute the eigenfunctions of the integral operator.

We believe that in the tomography setup, the eigenfunctions of the square-to-disk Slepian operator provide a linear space that naturally describes both the measured data and the reconstructed image. The well-localized nature of tomographic projections allow us to approximate them using only the eigenfunctions corresponding to eigenvalues close to 1 since these eigenfunctions are well-localized in the spatial box (slightly away from the boundary) while their Fourier transforms are supported in the disk (see [3, Sections 2.2-2.3] for details). In practice, this property leads to quadratures with controlled accuracy for functions band-limited within a disk

- **The exponents η$_m$ in equation (3.6) are defined by the roots γ$_m$ via η$_m$ =**

Fourier data, we discard them at the expense of introducing an additional error. The following approach aims to isolate such errors to the vicinity of singularities, which are responsible for the slow decay of the Fourier data and the mismatch between DFT and Fourier series coefficients.

The proximity of a node to the unit circle controls the frequency contribution of that node while the position of the corresponding pole (of the rational approximation) is directly associated with the location of a singularity [6]. Therefore, the impact of removing nodes just outside the unit disk should be localized to neighborhoods of singularities. However, when we remove nodes from just outside the unit circle and use the ℓ^2 norm to calculate the weights via (3.9), the error spreads out to a large neighborhood of the singularity as illustrated in Figures 4.1 (a)

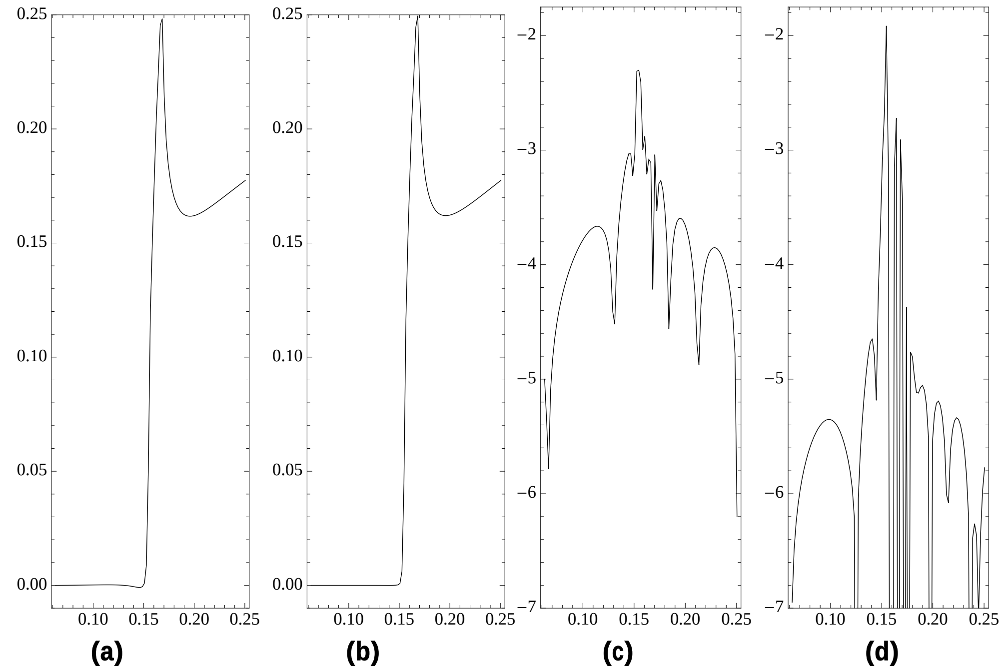

Figure 4.1. **Rational approximation of a projection in the vicinity**

$$W(\rho) = \sin^2\left(\frac{\pi}{4}\rho - \frac{\pi}{2}\right), \quad \rho \in [0,2]. \tag{5.3}$$

In comparison, within the FBP algorithm, the bandlimit c (corresponding to the measured data) is enforced by e.g., the Shepp-Logan filter. Since we first extend to the larger bandlimit c_{new}, and then apply the filter (5.3), the impact of the filter on the measured data of bandlimit c is significantly reduced, since the filter mostly modifies the extended part of $\widehat{g}^{ext}$.

Therefore, we obtain

$$\widehat{g}^{bl}(\rho,k) = \widehat{g}^{ext}(\rho,k)\,W(\rho), \tag{5.4}$$

where the window is specified in (5.3). Since the image is a real valued function, we define

$$\widehat{g}^{bl}(-\rho,k) = \overline{\widehat{g}^{bl}(\rho,k)} \tag{5.5}$$

for each projection, $k = 0,\ldots,N_\theta - 1$ and then sample $\widehat{g}^{bl}(\rho,k)$ on the diameter using quadrature nodes $2\rho_\nu$, $\nu = -N_\rho,\ldots,N_\rho$ described in Section (3.2) (we may also choose a quadrature with an even number of nodes on the diameters).

The final step of the algorithm uses the USFFT [11, 2, 26] with input values $\widehat{g}^{bl}(2\rho_\nu,k)$, $\nu = -N_\rho,\ldots,N_\rho$ and $k = 0,\ldots,N_\theta - 1$ to produce an image. This step

6. Numerical examples

We now analyze the impact on image resolution of the rational approximation of projections and compare the new PQI algorithm with the FBP algorithm. Followobserve that the PQI algorithm achieves a significantly improved resolution without introducing additional artifacts.

This also allows us to compare the output of our algorithm with that of the FBP algorithm on augmented projections. We see no significant difference in the reconstructions Figure 6.3 (a) and Figure 6.2 (a). A comparison of the reconstruction errors, Figure 6.3 (b) and Figure 6.2 (b) also shows no significant difference.

6.2. Zooming in on details In order to demonstrate the increased resolution, we zoom in on two areas of the reconstruction. The locations of these areas are shown in Figure 6.3 (a). In Figures 6.4 and 6.5 we compare images near the center of the phantom using the FBP and the PQI algorithms, respectively. Figure 6.4 compares a 32×32 pixel patch (obtained from the original data set of 512 projections with 512 samples each and extracted from 512×512 pixel reconstruction via FBP) and a 64×64 pixel patch extracted from 1024×1024 reconstruction using the FBP on augmented data. Similarly, in Figure 6.5, we compare the same 32×32 pixel patch with a 64×64 patch extracted from 1024×1024 reconstructed image using the PQI algorithm. A similar comparison is shown in Figures 6.6 and 6.7 but zooming into a different section of the Shepp-Logan phantom.

We observe that higher resolution is not accompanied by any additional artifacts and results in visibly sharper images.

6.3. Noisy examples To test the stability of approximation by rational functions in the presence of noise, we add (to each projection) Gaussian white noise with zero mean and standard deviation of $2.5 * 10^{-}$. The noise level is of the same order as the smallest features captured by the projections. In all experiments involving noise we used the threshold $\sigma_M / \sigma \leq 2 * 10^{-3}$ to find rational approximations (see Remark 3.4). We construct rational approximations for each noisy projection and [illegible]

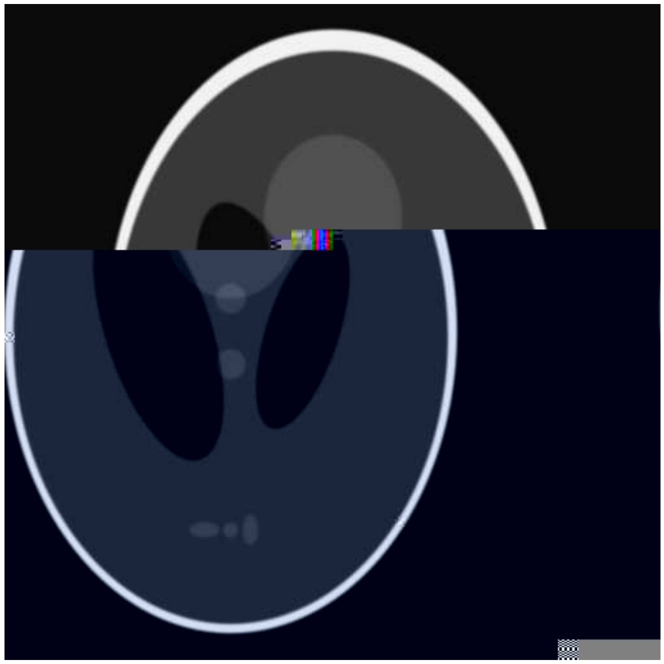

(a)

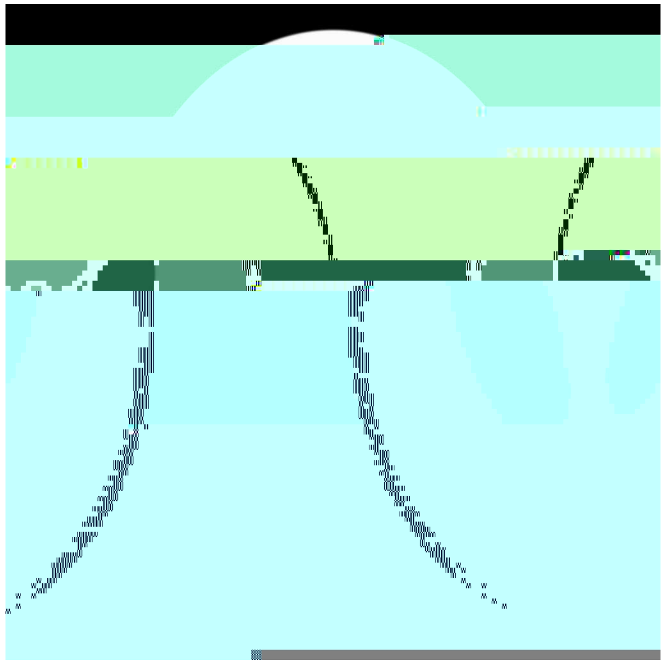

(a)

(b)

Figure 6.2. **A 1024 $\times$ 1024 reconstructed image of the Shepp-Logan phantom via the FBP algorithm using projections (with twice as many samples) generated by near optimal rational approximation (a) and the corresponding error (b). Gray scales are the same as in Figure 6.1 which should be used for comparison.**

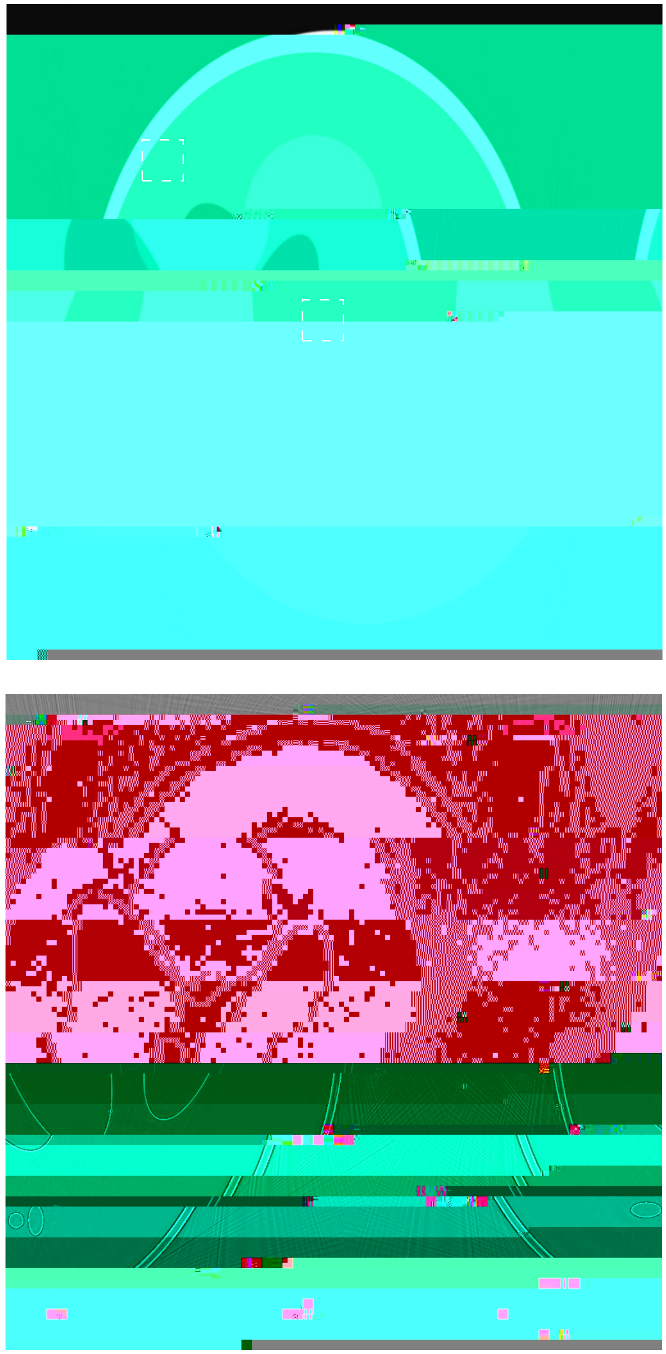

(a)

(b)

Figure 6.3. **A 1024 × 1024 reconstructed image via the PQI algorithm of Section 5 (a) and the corresponding error (b). The gray scales are the same as in Figures 6.1 and 6.2, which should be used for comparison. The two boxes in (a) outline areas of the reconstructed image on which we zoom to examine the reconstruction at a pixel level.**

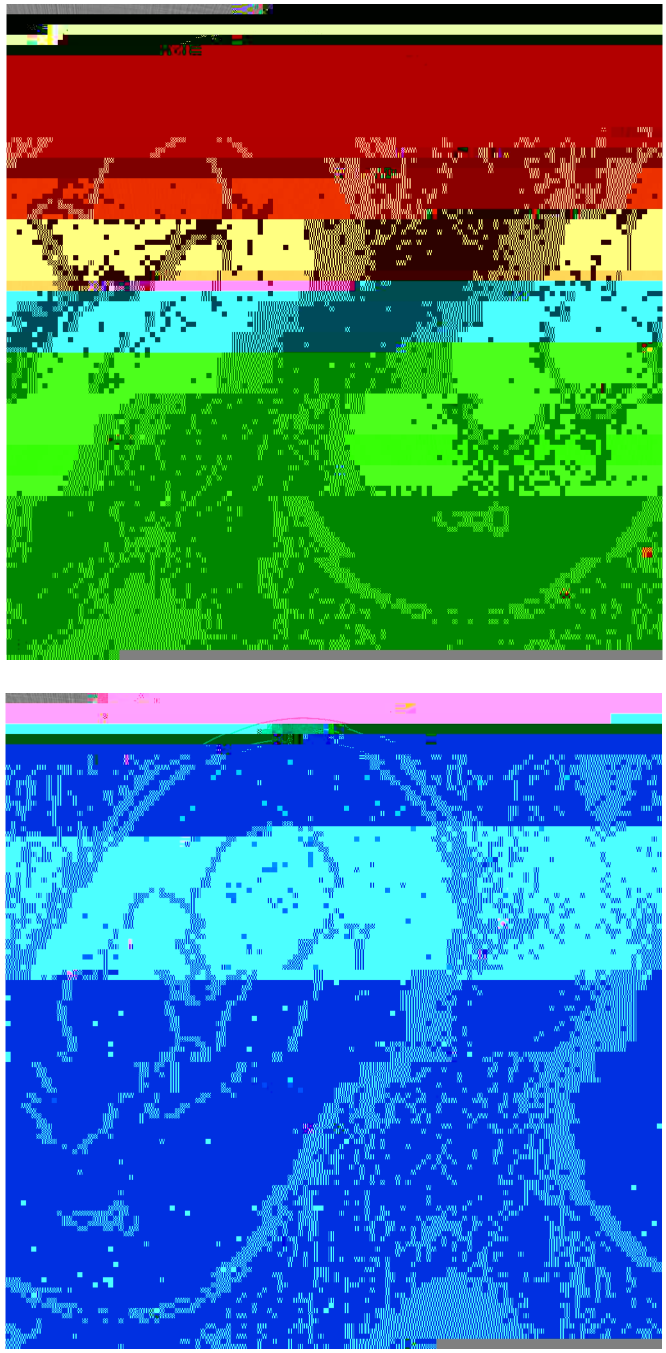

(a)

(b)

Figure 6.8. **Comparison of errors of 1024 $\times$ 1024 reconstructions in Figure 6.2 (via the standard FBP applied to noiseless data) (a) and the same data with added Gaussian noise (b). We observe that the Gaussian noise creates a speckle component in the error.**

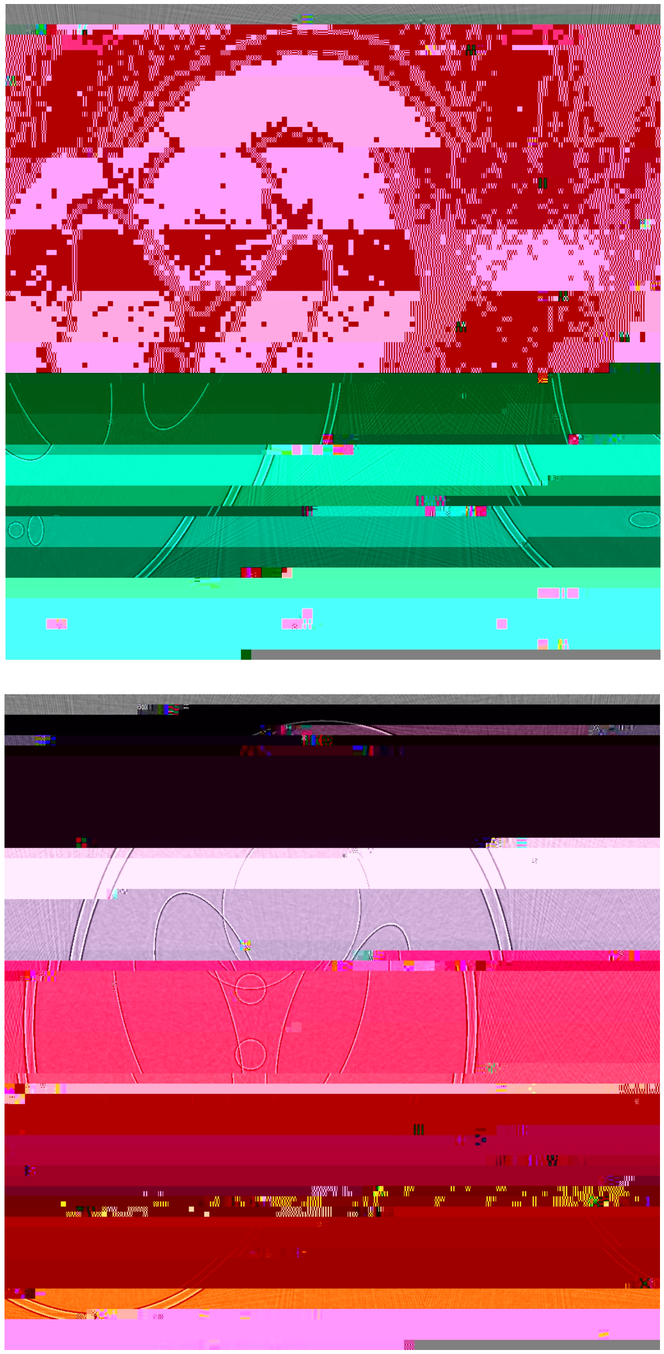

(a)

(b)